Geometric phases in soft materials
Abbaszadeh, H.

Citation

Abbaszadeh, H. (2021, January 27). *Geometric phases in soft materials. Casimir PhD Series*. Retrieved from https://hdl.handle.net/1887/139164

Version:	Publisher's Version
License:	
Downloaded from:	https://hdl.handle.net/1887/139164

Note: To cite this publication please use the final published version (if applicable).

Cover Page

Universiteit Leiden

The handle http://hdl.handle.net/1887/139164 holds various files of this Leiden University dissertation.

Author: Abbaszadeh, H.
Title: Geometric phases in soft materials
Issue date: 2021-01-27

Chapter 5.

Edge modes in rotating Rayleigh-Bénard systems

Pattern forming systems are a hallmark of studying non-equilibrium physics. A system that is driven out of equilibrium and is starting from a thermally fluctuating state finally reaches a state with clearly distinguishable patters on a mesoscopic or macroscopic scale. The patterns can be stationary or time-dependent. This time dependence can range from coherent periodic behaviors or traveling waves to chaotic motions.

Here, we consider a well-studied example of these out-of-equilibrium systems that is called the Rayleigh-Bénard convection [119]. An experimental setup for this phenomenon is a cylindrical cell filled with a fluid that is exposed to two heat baths with different temperatures, the below plate being the hottest one, see Fig. 5.1(a). The buoyancy force resulting from this temperature difference leads to a heavier fluid near the top plate, which then together with the gravity force induce flows in the fluid. If temperature and gravity overcome the viscous forces of the fluid, convective flows start to emerge. This competition between drive and viscous forces is expressed quantitatively by the Rayleigh number

$$\text{Ra} = \frac{\alpha g d^3 \Delta T}{\nu \kappa},\tag{5.1}$$

where α is the thermal expansion coefficient, g is the gravitational acceleration, d is the vertical length scale, ν is the kinetic viscosity, and κ is the thermal diffusivity of the fluid. The critical value for this parameter indicates the point beyond which convection takes place. The qualitative description above can be modeled by a set of modes for such systems which are linearly instable above

the convection threshold. These unstable modes grow out of the thermally fluctuating states. However, this growth will have to stop eventually, as the nonlinearities get involved and saturate the growth, steering the system towards its steady state.
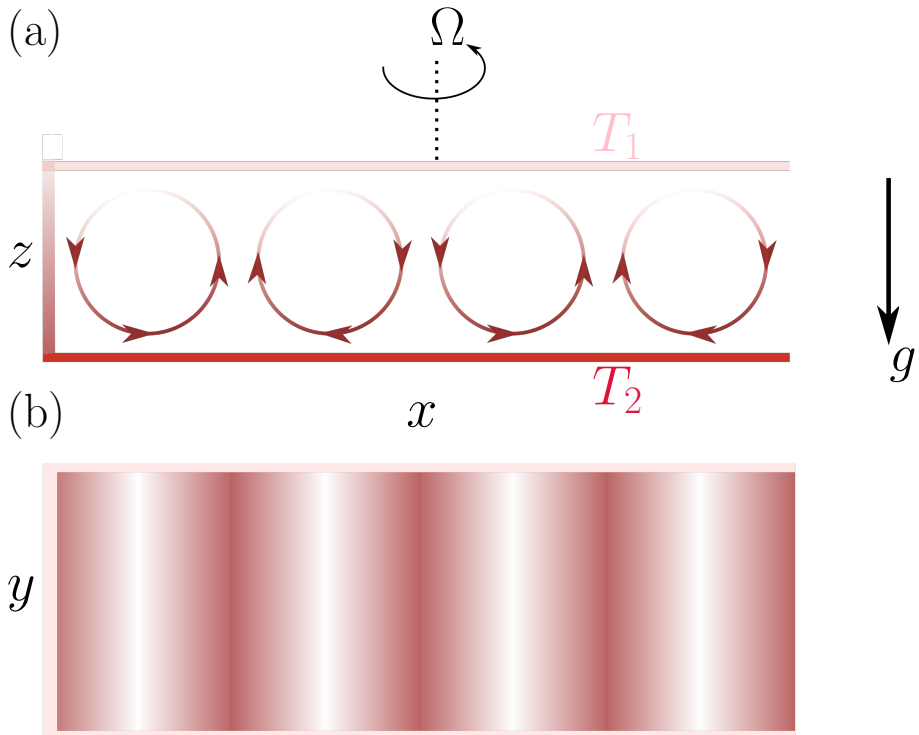

Figure 5.1: (a) A schematic picture of the Rayleigh-Bénard convection cell from the side view. The temperature field of the flow as well as that for the top and bottom plates is depicted by the intensity of the red color ($T_2 > T_1$). Above a critical point, the rolls start to develop and lead to the heat convection. A rotating Rayleigh-Bénard can be achieved by an angular velocity Ω. Panel (b) is a snapshot of this system from the top and shows a stripe pattern.

An important aspect of the description above is a competition between the modes themselves: the modes with maximum growth rates grow faster and thus eventually dominate the final steady state. At the onset of the instability transition, there is a finite number of most unstable modes of the system. These modes induce a slower length- and time scale into the system through their wavelength and frequency.

These slow characteristic length- (and time- for the case of oscillatory steady states) scales make the steady states periodic in space (and time). This explains the important observation of the system's self-organization towards patterns of hydrodynamic instabilities in the Rayleigh-Bénard experiments. There is a variety of shapes and types patterns that can appear in the Rayleigh-Bénard system [106]. The simplest of such patterns are in the shape of stripes (or rolls), as depicted in Fig. 5.1. Each roll is created as a result of the balance between the buoyancy forces and the dissipation due to viscosity and temperature diffusion between cold and hot flows. The separation of the rolls is determined by the characteristic length scale of the most unstable mode of the system. Also, depending on the frequency, this steady state pattern can be stationary or oscillatory in time.

Rotating Rayleigh-Bénard experiments are considered as simplified models for internally rotating convection systems, with examples in geophysical and astrophysical systems [105]. In a rotating Rayleigh-Bénard cell, the so-called wall modes, which are localized modes close to the vertical boundaries, precess in forms of unidirectionally moving traveling waves [142, 146, 179]. The observation of this unidirectional traveling edge states, along with similar observations in other pattern forming systems [58], suggests a possible relation between these modes and the topologically protected chiral edge modes in topological insulators. Inspired by the observation of topological modes in other hydrodynamics systems with Coriolis force [20, 38] or with chiral active constituents [19, 35], we became interested in studying such a possible explanation for the traveling wall modes in the rotating Rayleigh-Bénard experiments. For example, in a rotating Rayleigh-Bénard cell with a rotation rate $\mathbf{\Omega}$, the Coriolis force $\rho\mathbf{\Omega} \times \mathbf{v}$ also breaks the chiral symmetry between right and left moving flows along the azimuthal direction [140, 142]. This chapter is a summary of this ongoing study that has been done in last two years.

Recently, Favier and Knobloch obtained a strong evidence of the robustness of the traveling wall modes by showing their immunity from extreme boundary deformations through full numerical simulations [4]. These flow patterns of wall modes seem to exist for a wide range of Rayleigh numbers beyond the onset of the convection transition, i.e. ranging from a stable to chaotic bulk [9, 11]. However, a theoretical explanation is yet lacking for these observations. In this chapter, we report our progress in formulating a theoretical framework for such a theoretical investigation.

We use a generalized Swift-Hohenberg equation to effectively describe the behavior of the rotating Rayleigh-Bénard cell [106, 174]. Using these equations we reproduce a variety of phenomena, such as pattern shapes. Furthermore, we linearize a one-dimensional Swift-Hohenberg model around its steady state and use periodic boundary conditions to extract its band structure. Furthermore, by calculating the Zak phase of these bands we find signs of nontrivial topology in this band structure and relate this to an up-down symmetry breaking of the model. To describe the topology of the wall modes in a rotating Rayleigh-Bénard experiment, one needs to consider a two-dimensional model, such as the generalized Swift-Hohenberg model. We numerically verify that this model leads to wall modes and traveling states, as well as their robustness to rough boundary deformations.

An important distinction of the Rayleigh-Bénard system with the other topological hydrodynamic examples above is the dissipative and the nonlinear aspects that are needed for pattern formation. With recent formulation of nonlinear Zak phases and their relation to topological states in nonlinear systems [10], the future focus of this project will be in generalizing our results to describe the topology of the full nonlinear models of the rotating Rayleigh-Bénard experiments. Also, the dissipative aspect introduces non-Hermiticity in the dynamics of this model [8], for which one needs to consider the topology of the non-Hermitian systems [1, 2, 31, 32].

5.1   Model equations

We consider a generalized Swift-Hohenberg equation [106],

$$\partial_t u = ru - (1 + \nabla^2)^2 u + hu^2 - g_1 u^3$$
$$+ g_2 \mathrm{rot}\left([\nabla u]^2 \nabla u\right) + g_3 \mathrm{div}\left([\nabla u]^2 \nabla u\right), \qquad (5.2)$$

where u represents the physical field such as velocity or temperature, and r is proportional to the reduced Rayleigh number

$$\epsilon = \mathrm{Ra}/\mathrm{Ra}_c - 1, \qquad (5.3)$$

where Ra is the Rayleigh number and Ra_c is its critical value corresponding to the transition to convection transition. When $h = g_2 = g_3 = 0$, this equation is called the Swift-Hohenberg equation [174], which despite its simplicity (compared to full Navier-Stokes description of these systems) recreates some of the complex phenomena associated with the Rayleigh-Bénard experiment [140, 143, 162]. We now discuss the additional terms in the generalized model above.

5.1.1 Symmetries of the Rayleigh-Bénard system

The Swift-Hohenberg model has inversion symmetry that is between up and down flows, i.e. under $u \rightarrow -u$. This symmetry is violated once, for example, the fluid properties are temperature dependent, and thus the coefficients of the model change in the vertical direction as the higher flows are colder [184]. This is called the non-Boussinesq regimes [180] and can be mimicked in the model equation by adding a quadratic term which now breaks the up-down symmetry.

Apart from hexagonal patterns [145, 154, 181], symmetry breaking can bring new effects in the types of modes that can exist in a system. Let us focus for now on a quasi-1d model by considering stripe patterns in a Rayleigh-Bénard cell. A cross-sectional view of this flow pattern is shown in Fig. 5.2. We explained above that near the threshold one can consider a separation of scales by looking at the amplitude of slowly varying modes. Therefore, this picture can be qualitatively thought as amplitudes of a wavefunction that are located on the center of each roll and thus map this system into a lattice model. In a very qualitative way, let us consider that each roll interacts with a neighboring roll by passing alongside it ♠. A non-Boussinesq regime can then be translated into a different coupling between the neighboring rolls that go upward and the one between downward flows. Thus, in this naive picture one can see that this system might be mapped to a SSH chain [172].

Mapping to a SSH chain might help with the existence of wall modes in Rayleigh-Bénard systems. However, we also tend to explain the traveling wall modes when such systems start to rotate. Therefore, we consider the rotational symmetry breaking of the Rayleigh-Bénard system with the introduction of rotation to the convection cell. This is also called a chiral or azimuthal symmetry in the literature [140, 142] and is the system's symmetry under flipping the horizontal velocities of the fluid. The term chiral symmetry breaking here is used differently from the chiral symmetry that corresponds to the sublattice symmetry in a SSH chain, e.g. in the chapter 2. Here, this symmetry can be understood from the observation of unidirectionally moving wall modes in the rotating Rayleigh-Bénard system. That is a reminder of the presence of chiral edge modes in the quantum Hall effect, and was our key motivation to try to understand the possible connections between the two systems. In a rotating cell the Coriolis force breaks this symmetry between right moving and left moving modes. In Eq. 5.2, the rotation term is the consequence of

---

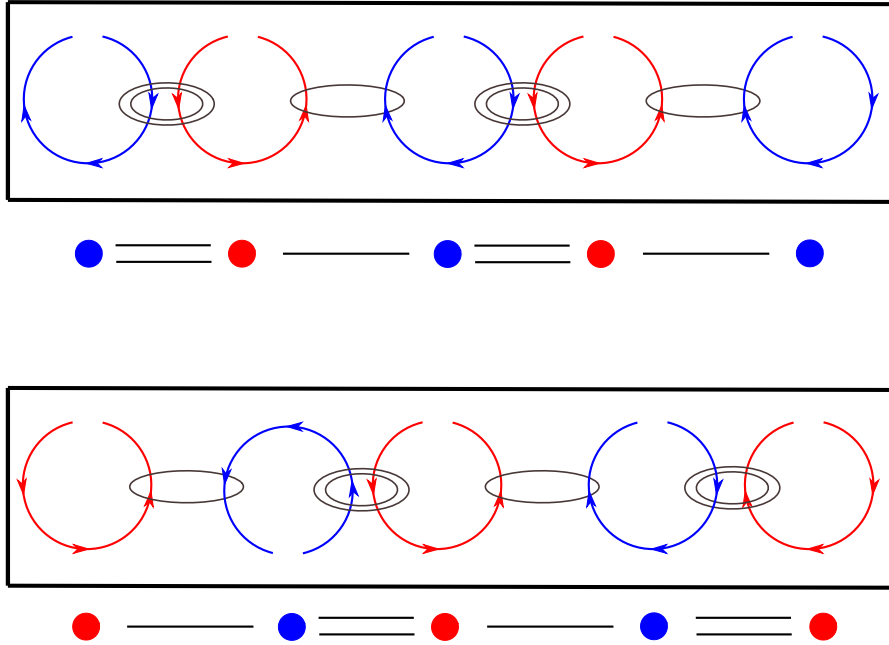♠We will try to quantify this approach later in this chapter.

Figure 5.2: A qualitative map between a 1d Rayleigh-Bénard pattern forming system in the non-Boussinesq regime and the SSH chain. Putting a boundary to the system can break the translation symmetry of the effective lattice picture. This lack of the translation symmetry is a crucial factor in finding a topological edge mode in a SSH chain.

such force in the system and g_2 is proportional to the rotation rate $\mathbf{\Omega}$. The symmetry breaking of the Coriolis force is also present in the emergence of topological modes in ocean waves [38]. Topological modes are also found in fluids which break this symmetry through chiral constituents [19, 35, 58].

The last term in Eq. 5.2 is a potential term that is of the same order as the rotation term and becomes relevant in some regimes [158]. In our attempt to understand a minimal model to describe a rotating Rayleigh-Bénard cell, we drop this last term in our simulations by setting $g_3 = 0$.

5.1.2 Simulations of the generalized Swift-Hohenberg equations

We simulate generalized Swift-Hohenberg model, Eq. 5.2 using Dedalus, a package for solving partial differential equations based on spectral methods [3]. The convective domain is separated from a non-convective one via a change in the value of r. We perform these simulations for both quasi-1d and circular geometries of the convective domain. In our simulations, we observe the regimes of the system where the pattern is moving unidirectionally along the edge, while the bulk patterns are stationary up to local vibrations and not moving in a specific direction, see Fig. 5.3, where the bottom insets in panels (b)-(d) depicts a tracking of the hexagons. We observe this behavior for both stripe and hexagonal patterns. Here, we only focus on the regime of hexagonal patterns in order to avoid complicated behavior of the partially moving stripes in terms of defect creation and annihilation.

Furthermore, in our simulations we observe that the patterns are robust against boundary deformations. The hexagons at the domain wall act as unidirectionally moving particles without being backscattered from the obstacle at the boundary. These results reproduce the results of Ref. [4] using the generalized Swift-Hohenberg model.

5.2 Linear dispersion relation

Let us consider a general pattern forming system that is described by a nonlinear deterministic dynamics

$$\partial_t \psi = \mathscr{N}[\psi],$$ (5.4)

where $\mathscr{N}$ is in general a nonlinear operator. Let us now constraint the systems to have a steady state that is obtained by $\mathscr{N}(\psi_{\mathrm{ss}}) = 0$ for spatial patterns♠. For any perturbation around this steady state we have

$$\partial_t \psi = \mathscr{L}(\psi - \psi_{\mathrm{ss}}) + \text{nonlinear terms},$$ (5.5)

where

$$\mathscr{L} = \frac{\partial \mathscr{N}}{\partial \psi}\bigg|_{\psi_{\mathrm{ss}}}$$ (5.6)

♠For an instability pattern, one can generalize this definition to non-stationary steady states by requiring a frequency term in the right-hand side.
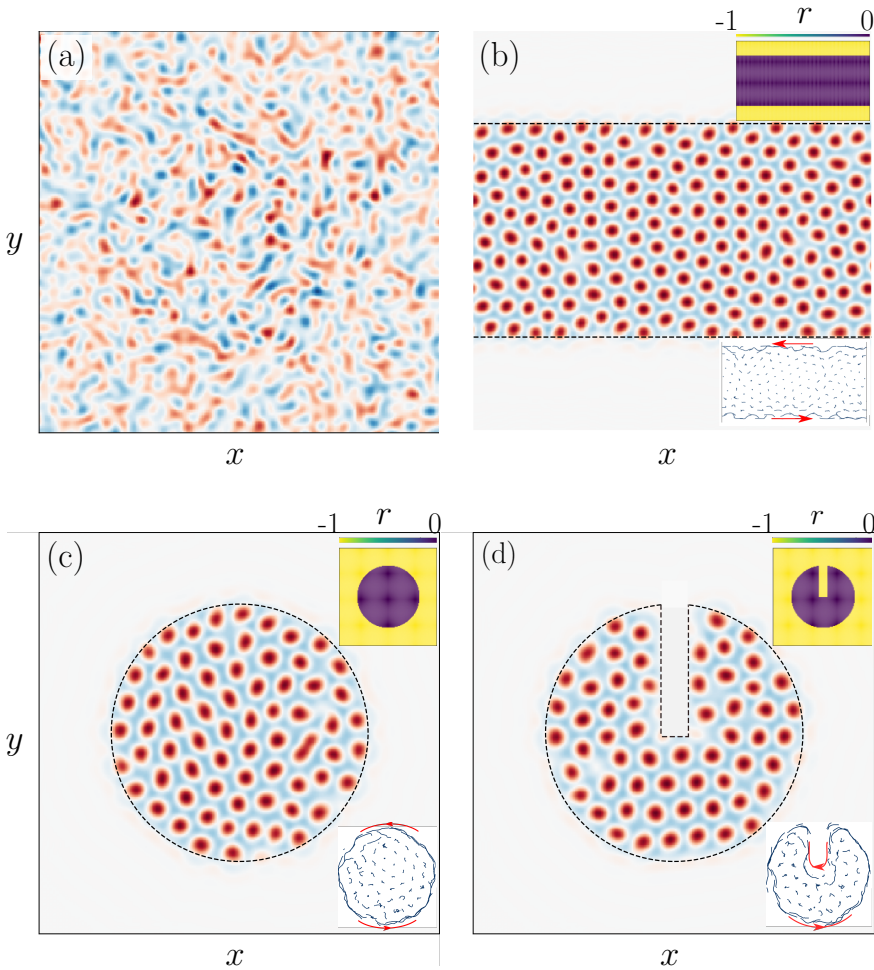
Figure 5.3: Simulation of the Rayleigh-Bénard system using Swift-Hohenberg model, Eq. 5.2. (a) The initial state is a thermal fluid. Hexagonal patterns appear in a quasi-1D (b) or a circular (cylindrical) setup. The top inset shows the r field that is used in the simulations to build a domain wall between ordered and non-convective ($r < 0$) states. The bottom inset shows a track of the hexagons in these simulations. The red arrows in these insets show the pattern movement direction at the walls. As can be seen in (b)-(c) the hexagons close to the domain wall move along the wall, while the ones in bulk vibrate. (d) Robustness of the wall modes in a rotating Rayleigh-Bénard systems with respect to boundary deformations. For these simulations we used $h = 1$, $g_1 = 1$, $g_2 = 0.1$, $g_3 = 0$, $r_{\text{inside}} = 0.3$, and $r_{\text{inside}} = -1$.

is the linearized operator that describes the dynamics of the system around its steady pattern. Here, we extract this dispersion relation by directly applying a Fourier transformation to the linear operator $\mathscr{L}$.

5.2.1 Fourier response and edge modes in 1d Swift-Hohenberg model

With a qualitative approach we reasoned that the breaking of the up-down symmetry in the 1d Swift-Hohenberg model in the non-Boussinesq regime, described by

$$\partial_t u = (r-1)u - 2\partial_x^2 u - \partial_x^4 u - g_1 u^3 + hu^2 \tag{5.7}$$

can be similar to the chiral symmetry breaking in an SSH chain.

Here we quantitatively test this idea using the linear stability analysis method that is described before in Eq. 5.5. We look at the spectrum of the excitations around the steady state of the model, given it exists. To do so, we first linearize the Swift-Hohenberg equation around its steady state

$$\partial_t \delta u = (r-1)\delta u - 2\partial_x^2 \delta u - \partial_x^4 \delta u - 3g_1 u_{ss}^2(x)\delta u + 2hu_{ss}(x), \tag{5.8}$$

where $\delta u(t,x) = u(t,x) - u_{ss}(x)$ is the perturbation around the steady state. Now we move to the Bloch space by writing $\delta u(x) = \mathrm{e}^{-ikx}v(x)$, where $v(x+2\pi) = v(x)$. The equation of motion for v reads $\partial_t v(t) = \mathscr{L}(k)v$, where $\mathscr{L}(k)$ is a differential operator acting on periodic functions. The real and imaginary values of the spectrum of this operator give the growth rate and the frequency of the excitations around the steady state. In Fig. 5.4 we show the growth rates for some values of r, g, and h. The excitations are non-oscillatory in this model, i.e. all frequencies are zero and the patterns are stationary.

We further examine the topological nature of these excitations by computing the Zak phase which is the integral of the Berry connection over the first BZ, and is determined for a single band i as [149]

$$\gamma_i = \int_{1^{st}\ \mathrm{BZ}} A_i. \tag{5.9}$$

Interestingly, we observe that when $h \neq 0$ gaps start to open in the band structure of $\mathscr{L}(k)$, as shown in Fig. 5.4. Alos, the Zak phases for the gapped bands are quantized and in some cases are $\pm\pi$, which is an indication of the topological non-equivalence of these bands with the ones with $\gamma = 0$.
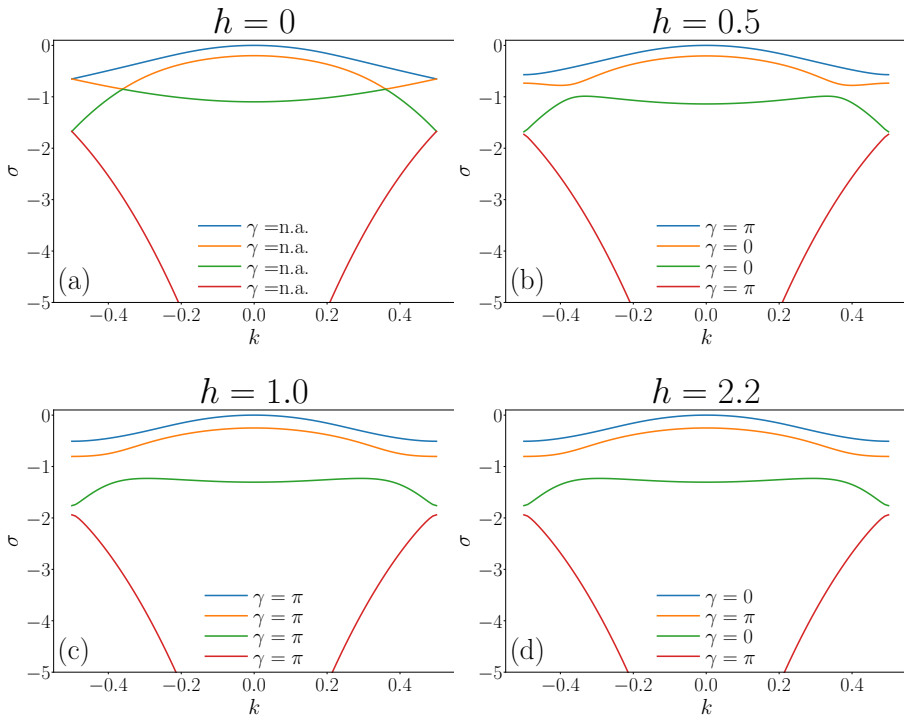
Figure 5.4: Growth rates, σ, of the modes in the linear stability analysis of the Swift-Hohenberg model around its steady state for various values of the up-down symmetry breaking parameter h. The horizontal axis shows the modes wavenumbers throughout the first Brillouin Zone. Legend shows the calculated Zak phase for each of the bands. We observe that the Zak phase is quantized for $h \neq 0$. For $h = 0$, the Zak phase is undefined as the band structure is not gapped.

We further build a domain wall in this system to examine the effect of this topological non-equivalence and check whether it leads to any domain-bound mode, as in the Jackiw-Rebbi model [163, 175]. In figure 5.5 we show the results of this numerical investigation for a choice of parameters $r = 0.1$, $g_1 = 2$, and the effective wall is between regions with $h = 1.2$ and $h = 2.0$. In panel (a), we show the projected growth rate bands for the two systems at different sides of the domain wall as well as the calculated Zak phases of each of the bands. In each shared gap (some of them can be very small) we indicate the observation of a domain-bound mode by ⋈, and use x otherwise. Fig. 5.5)(b) shows an the edge mode that corresponds to the non-trivial gap between the two sides of the domain wall.
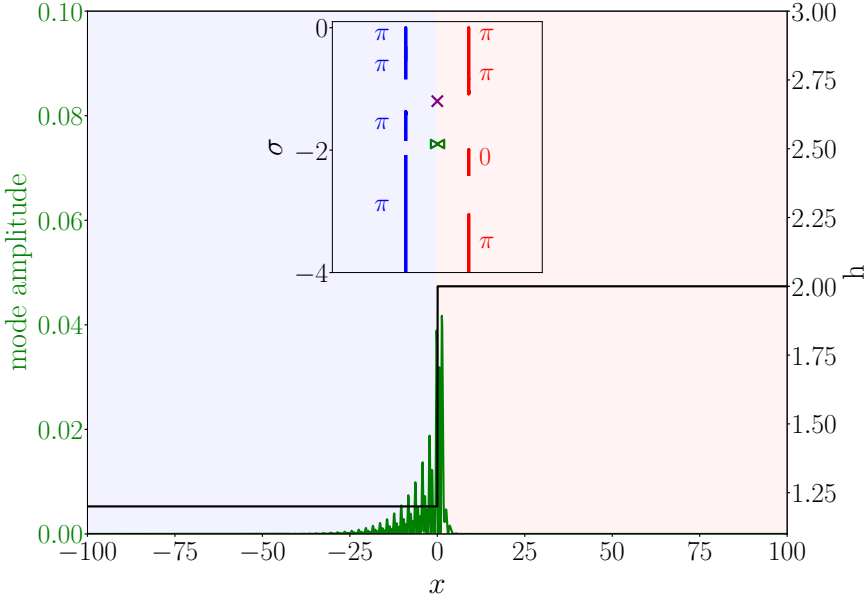
Figure 5.5: Search for domain-bound modes in the Swift-Hohenberg model with domain wall in the reflection-symmetry breaking parameter h. Inset shows a projection of the band structure for the linearized Swift-Hohenberg model for two regions. We search for the presence of the domain-bound modes induced by the domain wall between the two systems, and mark the presence of such modes in a shared gap with ⋈ and the absence with x. The corresponding mode to the ⋈ is localized at the boundary between the two domains and is exponentially decaying in intensity away from the domain wall.

These observations, although promising, are not a complete proof of a map between this system and a Jackiw-Rebbi model [175]. First of all, we examine a bulk-boundary correspondence between the presence of non-trivial gaps and the existence of domain-wall modes via direct numerical calculations. A systematic proof of the bulk-boundary correspondence above will be subject of further investigations.

Furthermore, it is not clear if the observation above proves a connection to other domain-wall systems, e.g. Jackiw-Rebbi model. In the Jackiw-Rebbi model, as we also saw in the second chapter of this thesis, the modes that localize at the domain wall of the system are polarized. This polarization

depends on the specific system and can for example be a mode's spin or sublattice degree of freedom. The existence of such polarization for the domain-bound modes in the Swift-Hohenberg equations that we derived above is yet to be understood.

Another concern is how to observe these edge modes, since all these edge modes are unstable with negative growth rates. One solution might be in the use of strong nonlinear terms at the boundary and larger perturbations around the steady state, similar to a pumping drive, such as in topological lasers [25, 27]. Having a negative growth rate from the stability analysis of the system around its steady state is inevitable by definition. Therefore, although getting to a topological band structure is plausible, we might still lose some of the physics of the problem by restricting ourselves to the linear regimes. In the rest of this chapter, we try to examine the topology of the system in nonlinear models. We then first start by a nonlinear regime of the problem very close to the threshold, where the separation of scales happens due to strong selection of most unstable modes in long-term dynamics. The formal description of this theory is through the amplitude expansion.

5.3 Nonlinear amplitude equations and system's discretization

At the threshold of the instability, the system starts to have a steady-state pattern. The state of the system around its steady state can be expressed as

$$\text{physical fields} = u^{\text{ss}}(t) + \sum_j A_j^{\text{ss}} e^{s_j t} \phi_j + \text{c.c.}, \tag{5.10}$$

where the perturbations around the steady state are expressed in the basis of the eigenmodes of the linearized operator, $\mathcal{L}$ with the corresponding eigenvalues $s_j = \sigma_j + i\omega_j$, where σ is the growth rate and ω is the frequency of each mode. Of all the modes in this expansion, the ones with the maximum growth rate contribute to the long-term dynamics of the system: these modes grow in amplitude to trigger the nonlinearities in the system.

Very close to the threshold, the modes with positive growth rates have a wavenumber very close to the one from the most unstable mode(s) at the onset. The state of the system is thus effectively described by this subset of modes. One can describe this system using the following perturbatively expansion [140]:

$$u_{\text{p}} = \epsilon^{1/2} u_0 + \epsilon^{3/4} u_1 + \epsilon u_2 + \cdots, \tag{5.11}$$

where ϵ is the distance from the threshold, and each order of the expansion can be written as

$$u_i(x, y, z, t) = e^{i\mathbf{k}.\mathbf{r}} A_i(X, Y, T) v(x, y, z, t) + c.c., \quad |\mathbf{k}| = q_c, \qquad (5.12)$$

where we separated the dynamics along the z direction from the amplitude A_i. Moreover, the spatial dynamics in the direction perpendicular to the top-bottom surfaces of the cylinder is also separated for patterns with characteristic wavenumber q_c. The amplitudes A_i are slowly varying envelopes that can mimic a periodic structure of stripes. That is close to a Bloch tight-binding description of a continuum wavefunction of a lattice in quantum mechanics. This approximation can lead to a discretized model of this complex system close to the threshold of pattern formation. In the situations where two or more modes constitute to a system's steady state, this effective discretized model might be helpful in describing the interaction of these modes. Examples of such systems are observed in Rayleigh-Bénard cells where square or hexagonal patterns become linearly more stable than the stripe instabilities [156, 164, 181].

The slow parameters X, Y, T are scaled spatial and temporal variables which should be deducted from the dynamics of the physical fields. They are such that $|\nabla_{\mathbf{r}} A| \ll |q_c A|$ and $|\partial_t A| \ll |\omega_c A|$, where $\omega_c = \omega(q_c)$ is the frequency of the most unstable mode. One can then reduce the dynamical model into finding the dynamics of the slowly varying envelopes A_i. By using this steps, we derive the following amplitude equations for the generalized Swift-Hohenberg model given by Eq. 5.2 (details in the appendix):

$$\partial_T A_0 = \left[1 + 4\left(\partial_X - \frac{i}{2}\partial_Y^2\right)^2\right] A_0 - (3g_1 - \frac{10}{3}h^2 + 3g_3)A_0|A_0|^2 \quad (5.13)$$

$$\partial_T A_1 = \left[1 + 4\left(\partial_X - \frac{i}{2}\partial_Y^2\right)^2\right] A_1 - 3g_1\left[A_0^2 A_1^* + 2|A_0|^2 A_1\right]$$

$$- 4ig_2\left[A_0\partial_Y|A_0|^2\right] + \frac{4}{3}h^2\left[A_0^2 A_1^* + 5|A_0|^2 A_1\right]$$

$$- 3g_3\left[A_0^2 A_1^* + 2|A_0|^2 A_1\right]. \qquad (5.14)$$

with slow variables

$$X = \epsilon^{1/2} x, \qquad\qquad\qquad (5.15a)$$

$$Y = \epsilon^{1/4} y, \qquad\qquad\qquad (5.15b)$$

$$T = \epsilon t. \qquad\qquad\qquad (5.15c)$$

The Eqs. 5.13-5.14 are in agreement with the the results obtained from the full Boussinesq equations [117]. There are some differences, including a second slower time scale $T' = \epsilon^{5/4}T$ which we did not fully explore, but that might have to do with the fact that the dynamics of the modes along the edge are happening at a different time scale compared to the other directions.

Amplitude equations above give a simplified nonlinear description of the Rayleigh-Bénard system's dynamics using the assumption that close to the threshold the fast and slow scale dynamics become separated. In the following, we will try to use this simplified model towards a description of the topology of the Rayleigh-Bénard system.

5.4   Band structure and topology of nonlinear systems

So far, we observed that the in 1d, the linearization of the Swift-Hohenberg model around its steady state solution leads to a band structure with Zak phases equal to $\pm\pi$. One issue with this approach is that, by definition the perturbations of the system around its steady state are decaying. Therefore, even if there are topological edge modes in such spectrum, it will not lead to the presence of this mode in the pattern forming system, except for a temporal rapidly deteriorating mode.

Following along this lines, we then could conclude that it might be more relevant to look for the topological properties of the modes in the full nonlinear regime. We then would like to see if the patterns, as the steady states of the system, are themselves topological modes of the fully nonlinear models.

To search for these modes in the context of band topology, we need to consider a generalized version of at least two concepts from the standard Hamiltonian problems. First, we need to generalize the band structure for a fully nonlinear Schrodinger equation, i.e. by solving the eigenvalue problem $H[u]u = \varepsilon u$ for a state-dependent Hamiltonian $H[u]$. We then would like to be able to repeat this for the Fourier components of this nonlinear Hamiltonian to obtain the energy spectrum in the Bloch space. Since H is state dependent, solving this equation in general can be very complicated. For example, a single plane-wave ansatz might be insufficient to diagonalize the Hamiltonian. Instead, we might want to generalize this to a more general space of functions using spectral methods.

There is however at least a family of such nonlinear Hamiltonians for which one can still use the Bloch Fourier transformation to find eigenstates of the system. That is, when the state-dependent terms are mere radial maps of the state u, such as $|u|^2 u$, etc. Models of this sort describe various physical system including examples from interacting Bose-Einstein systems described by Gross-Pitaevskii equations [130], KdV equations, nonlinear electronics and optics systems [6]. These systems are known to harbor solitary waves [144].

The second generalizations we will need to consider is how to characterize the topology in such nonlinear band structures. In a recent preprint [10], it was shown that adding nonlinearity to the Schrodinger equation can have an effect on the topological properties of the band structure. Particularly, this paper shows that adding nonlinearity to a SSH chain [172] can push the bands that are continuously evolved from the linear model, to revive an effective chiral symmetry (or a sublattice symmetry), even in the presence of the terms which break this symmetry. This result is then supported by generalization of Zak phase for nonlinear models, and showing that the quantization of the sum of these new phases revives as the nonlinearity becomes stronger in this system. Nonetheless, the nonlinear Zak phase continuously convert to the regular one in the linear models. Another interesting result in this paper was the presence of *in-gap solitons*, or the localized bulk states. The authors relate the presence of such modes to the emergent effective edges in the bulk due to the nonlinear terms and larger mode amplitudes. Considering these results, one would wonder whether the non-trivial Zak phases in the linearized Swift-Hohenberg model that we measured in the previous section is a hint to more general topological phases in the full nonlinear regime.

The non-linear band topology in the Ref. [10] above is examined for effective 1d models, whereas a rotating Rayleigh-Bénard systems is described by a two-dimensional model. An amplitude expansion for a two-dimensional model one can introduce a coupling term $G(\theta)$ between the modes with different orientation of their wavevectors [178]. This coupling can also break a rotational symmetry in the system, for example when it rotates ($G(\theta) \neq G(-\theta)$) [106]. These symmetry breaking terms are present in other timer-reversal broken topological insulators [100]. A more complete treatment of the rotating Rayleigh-Bénard systems in terms of topological properties of nonlinear systems will be subject of our future investigations.

5.5   Discussion and outlook

In this chapter, we discussed the results of an ongoing study on the topological phases in the rotating Rayleigh-Bénard system. Using numerical computations, we have observed topological Zak phases in the linearized band structure of the 1d Swift-Hohenberg model. An unknown fact about the model above is about the notion of polarization for these modes. As we have seen in the second chapter about the mechanical graphene, edge modes on Jackiw-Rebbi-type models are spin polarized (in that case sublattice polarized). The translation of this concept to a 1d Swift-Hohenberg model is still to be understood. Also, the bands of this linearized model are constructed by modes with negative growth rates. Hence, it is still not clear how these modes can have an effect on the non-transient dynamics of the system or can give rise to the topological edge modes, as suggested by recent numerical simulations [4]. Nonlinear drives at the boundary can have an effect on bringing the topological modes with negative linear growth rates into long-term dynamics of the Rayleigh-Bénard system.

Therefore, an explanation of the topological origin of the traveling states at the wall of the rotating Rayleigh-Bénard cell requires the generalization this result for the full non-linear equations. To do this, we first used a generalized Swift-Hohenberg model to reproduce the results of the Ref. [4] about the robustness of the wall modes in a rotating Rayleigh-Bénard system. A description of these wall modes will then probably require a generalization of the topological indices for a non-linear model. A first step will be to calculate the recently developed generalized Zak phase [10] for a 1d Swift-Hohenberg model, for which we already have a strong indication from the band topology of the linearized equations. We note that the topological indices for non-linear models are new concepts which we need to consider for the study of an out-of-equilibrium system.

Furthermore, A discretized model, as we described in §5.3, is useful in mapping the Rayleigh-Bénard system to a lattice model. This approach can be particularly useful for the 2d pattern forming systems. For example, It will be interesting to see how a three-coupled mode for hexagonal patterns are described with this theory, as for such patterns the amplitude description contains a chiral symmetry breaking term.

Also, a full description of such models will likely require non-Hermitian operators due to dissipation from the viscous forces. Looking forward, we will study a discretized model with the relevant symmetry-breaking terms. This model then will be both nonlinear and non-Hermitian. In future investigations, we will focus on the topological phases of the modes in such systems.

5.6   Appendix

5.6.1   Band structure of nonlinear Schrödinger/Gross-Pitaevskii equations

We discussed above that the generalization of the concept of band structure for the nonlinear Schrödinger can be far from straightforward. Especially, when the nonlinear terms are not radial, solving the eigenvalue problem will require a more general spectral method instead of Bloch waves. The nonlinear terms in the Swift-Hohenberg equation, even in the 1d version, are of this form. Thus, we will have to see how we should deal with the full diagonalization problem, when we decide to generalize this approach to this equation. Interestingly, when we linearize the model around the onset of the pattern formation system, i.e. for small values for the reduced Rayleigh number ϵ, it leads to a separation of scales in the form of amplitude equations, see Eqs. 5.13 and 5.14. When this separation happens, we no longer need to consider a mixture of Bloch modes in a spectral method in order to diagonalize the Hamiltonian. The amplitude equations are in form closer to Gross-Pitaevskii equations, or nonlinear Ginsburg-Landau equations. For example, it is shown that a complex Ginsburg-Landau equation can describe the one-way propagating mode in a rotating Rayleigh-Bénard cell [135].

Here, we derive the energy spectrum of the nonlinear Schrödinger equations that was considered in the nonlinear Landau-Zener tunnelling effect [126, 129]. Consider the following Hamiltonian of a two-level system:

$$H_{NLZ}\left[\begin{pmatrix} a \\ b \end{pmatrix}\right] = \frac{\gamma}{2}\sigma_z + \frac{v}{2}\sigma_x + \frac{c}{2}\left(|b|^2 - |a|^2\right)\sigma_z, \qquad (5.16)$$

which modifies the Hamiltonian of a standard Landau-Zener model by adding a nonlinear term which is proportional to the population difference of the system. The time-dependent version of this problem is achieved by considering $\gamma(t) = \alpha t$. When α is small compared to the energy gap, the evolution of the

system is expected to follow an adiabatic path. However, it is shown in the Ref. [129] that when $c > v$ this model predicts a tunneling even in the adiabatic limit. This nonadiabatic behavior appears as a result of loop structures in the band structure of the model.

We now give the steps to calculate the band structure of this model. We start by writing down the Schrödinger equation

$$i\partial_t a = \frac{v}{2}b + \left[\frac{\gamma}{2} + \frac{c}{2}\left(|b|^2 - |a|^2\right)\right]a, \tag{5.17a}$$

$$i\partial_t b = \frac{v}{2}a - \left[\frac{\gamma}{2} + \frac{c}{2}\left(|b|^2 - |a|^2\right)\right]b. \tag{5.17b}$$

The total population of the two bands $|b|^2 + |a|^2$ is constant (it is easy to check with the equations above). It is then possible to write

$$\begin{pmatrix} a \\ b \end{pmatrix} = e^{i\varphi_1} \begin{pmatrix} \sin\frac{\varphi}{2} \\ e^{i\theta}\cos\frac{\varphi}{2} \end{pmatrix}. \tag{5.18}$$

We define the population difference variable $s = |b|^2 - |a|^2 = \cos\varphi$. In terms of these new parameters, the Schrodinger equations converts to

$$\frac{i}{2}\dot{\varphi}\cos\frac{\varphi}{2} - \dot{\varphi}_1\sin\frac{\varphi}{2} = \frac{v}{2}e^{i\theta}\cos\frac{\varphi}{2} + \left[\frac{\gamma}{2} + \frac{c}{2}\cos\varphi\right]\sin\frac{\varphi}{2}, \tag{5.19}$$

$$\frac{-i}{2}\dot{\varphi}\sin\frac{\varphi}{2} - (\dot{\theta} + \dot{\varphi}_1)\cos\frac{\varphi}{2} = \frac{v}{2}e^{-i\theta}\sin\frac{\varphi}{2} - \left[\frac{\gamma}{2} + \frac{c}{2}\cos\varphi\right]\cos\frac{\varphi}{2}. \tag{5.20}$$

The real and imaginary parts of these equations lead to

$$\dot{s} = -\frac{dH_{\text{cl,NLZ}}}{d\theta} = -v\sqrt{1-s^2}\sin\theta \tag{5.21a}$$

$$\dot{\theta} = \frac{dH_{\text{cl,NLZ}}}{ds} = \frac{\gamma + cs}{1+s} \tag{5.21b}$$

$$\dot{\varphi}_1 = -\left[\frac{\gamma}{2} + \frac{c}{2}s\right] - \frac{v\sqrt{1+s}}{2\sqrt{1-s}}e^{i\theta} \tag{5.21c}$$

The eigensystem of the nonlinear Hamiltonian H_{NLZ} translates into $\dot{s} = \dot{\theta} = 0$ and $\dot{\varphi}_1 = \varepsilon$. Thus, the eigenmodes of the nonlinear Hamiltonian will correspond to the fixed points of the classical Hamiltonian [126, 137]

$$H_{\text{cl,NLZ}} = \frac{c}{2}s^2 + \gamma s - v\sqrt{1-s^2}\cos\theta. \tag{5.22}$$

Therefore, the eigenmodes of the nonlinear Hamiltonian correspond to

$$\theta^* = 0, \pi; \quad cs^* + \gamma = \frac{\pm v}{\sqrt{1 - s^{*2}}}, \qquad (5.23)$$

which leads to

$$f(s^*) = (1 - s^{*2})(s^* + \gamma/c)^2 = (vs^*/c)^2. \qquad (5.24)$$

The function f is positive in the interval$[-1, 1]$ and takes one maximum (two local maxima) when $|\gamma/c| > 1$ ($|\gamma/c| > 1$). Fiollowing a standard process, we find that Eq. 5.24 has two solutions for $v/c > 1$ and four solutions when $v/c < 1$ and $|\gamma| < \gamma_c$ for a critical γ_c value. These extra solutions to the nonlinear equations lead to loop shapes in system's energy spectrum. As a result, an adiabatic change in the Hamiltonian can lead to a nonadiabatic change in the ground state of the system which is what the authors call nonlinear Landau-Zener (NLZ) tunnelling.

5.6.2 A nonlinear SSH chain

We now try to study these generalizations in the context of a nonlinear SSH chain, following the results in the Ref. [10]. By starting from discrete system and considering the Bloch wavefunctions $\Psi_{A/B,j} = \Phi_{A/B,j} e^{ikj}$, the authors arrive to the following model:

$$H(\Sigma) = (J_1 + J_2 \cos k)\sigma_x + J_2 \sin k \sigma_y + h(\Sigma)\sigma_z + \frac{g}{2}I_2, \qquad (5.25)$$

where J_1 and J_2 are the hoppings in the chain, $h(\Sigma) = v + \frac{g}{2}[|\Phi_B|^2 - |\Phi_A|^2]$ contains the nonlinear term that is state dependent with g as nonlinearity strength, and v a chiral symmetry breaking term. Due to lack of the latter symmetry, in the usual case of the linear SSH the topological edge mode does not exist and the winding number of the Hamiltonian becomes ill defined. Interestingly, it is shown in Ref. [10] that in the presence of strong nonlinearity, the chiral symmetry effectively revives in the system's band structure and therefore it is possible to calculate a nonlinear Zak phase which is quantized.

Without going to further details, here we try to study the band structure for this system corresponding to the eigenvalue problem $H(\Sigma)\Phi = \varepsilon\Phi$, where $\Phi = \begin{pmatrix} \Phi_A \\ \Phi_B \end{pmatrix}$. First, it is easy to check that Eq. 5.25 leads to $|\Phi_A|^2 + |\Phi_B|^2 = 1$ (up to constants). We have

$$i\partial_t\Phi_A = v\Phi_A + \frac{g}{2}|\Phi_A|^2\Phi_A + (J_1 + J_2 e^{-ik})\Phi_B, \qquad (5.26a)$$

$$i\partial_t\Phi_B = -v\Phi_B + \frac{g}{2}|\Phi_B|^2\Phi_B + (J_1 + J_2 e^{ik})\Phi_A. \qquad (5.26b)$$

These equations are similar in structure to the NLZ problem, Eqs. 5.17. Using the same method as above we find

$$\dot{s} = -\frac{dH_{\text{cl,NSSH}}}{d\theta} = -2\sqrt{1-s^2}\left[J_1\sin\theta + J_2\sin(\theta - k)\right], \qquad (5.27a)$$

$$\dot{\theta} = \frac{dH_{\text{cl,NSSH}}}{ds} = 2v - \frac{g}{2}s + \frac{2s}{\sqrt{1-s^2}}\left[J_1\cos\theta + J_2\cos(\theta - k)\right], \quad (5.27b)$$

$$\varepsilon_k = -\dot{\varphi}_1 = v + g\frac{1-s}{4} + \sqrt{\frac{1+s}{1-s}}\left[J_1\cos\theta + J_2\cos(\theta - k)\right], \qquad (5.27c)$$

where $H_{\text{cl,NSSH}} = 2vs - \frac{g}{4}s^2 - 2\sqrt{1-s^2}\left[J_1\cos\theta + J_2\cos(\theta - k)\right]$. Here one needs to diagonalize the system for each wavenumber k in order to obtain a band structure. This calculation leads to the loop shapes in the band structure of the model in some regions of the BZ in the strong nonlinear regimes [10].